

# A Bidirectional Hybrid Switched-Capacitor DC-DC Converter with a High Voltage Gain

Dan Hulea

Department of Electrical Engineering  
Politehnica University of Timisoara  
Timisoara, Romania  
dan.hulea@student.upt.ro

Nicolae Muntean

Department of Electrical Engineering  
Politehnica University of Timisoara  
Timisoara, Romania  
nicolae.muntean@upt.ro

Mihaita Gireada

Department of Electrical Engineering  
Politehnica University of Timisoara  
Timisoara, Romania  
mihaita.gireada@student.upt.ro

Octavian Cornea

Department of Electrical Engineering  
Politehnica University of Timisoara  
Timisoara, Romania  
octavian.cornea@upt.ro

**Abstract**—This paper presents a new non-isolated bidirectional hybrid switched-capacitor DC-DC converter (BHSC) which achieves a high voltage conversion ratio. The hybrid characteristic is due to the switched capacitor cell that is inserted into a conventional buck/boost bidirectional converter, which also helps achieve the high conversion ratio. Apart from the high conversion ratio, the switched cell also helps reduce all passive components and the stress on the active switches, all without interrupting the input to output ground path. The stability of the converter is also addressed by using the state space averaging method (SSA), prior to the actual construction of the converter, in order to design the passive components so that possible instabilities that might occur are eliminated. The simulation results are used to confirm the initial theoretical considerations.

**Keywords**— dc-dc power converters, bidirectional, high conversion ratio, non-isolated, stability.

## I. INTRODUCTION

Bidirectional high ratio converters are beneficial in applications where a large voltage ratio between the input and output are present, such as in microgrid applications in storage applications [1]–[3] or as an interface converter [4], [5] or for electric vehicles in vehicle to grid configuration [6], [7], or supercapacitor storage [8], [9].

High ratio converters are especially beneficial in applications where supercapacitor storage is used, as the voltage of the supercapacitor varies proportionally to the square root of the stored energy, so a large variation is needed for a better utilization of the supercapacitor [10], [11].

The common ground is also beneficial in order to parallel multiple converters or to translate the topology into a multi-level one [12].

## II. CONVERTER TOPOLOGY AND ANALYTICAL DESCRIPTION

### A. Converter Topology

The proposed converter is a hybrid DC-DC converter as it uses switched capacitor cells, initially proposed in [13], and by doing so it achieves a higher conversion ratio, useful for a wider operating voltage. The topology is based on the unidirectional buck converter, enhanced with a switched capacitor cell, topology which was tested experimentally in the literature in [14].

The proposed converter, shown in Fig. 1, is a modified bidirectional buck/boost converter with the bidirectional

switched capacitor cell at the high voltage side. In comparison to other high ratio converter, such as, [15], [16], the proposed converter also has a common ground between the input and output signal which is a beneficial feature in many applications. In comparison to other topologies, [10], [17], with same conversion ratio, the proposed one uses an additional transistor, but as it is shown in the following sections, the total active switch stress is lower.

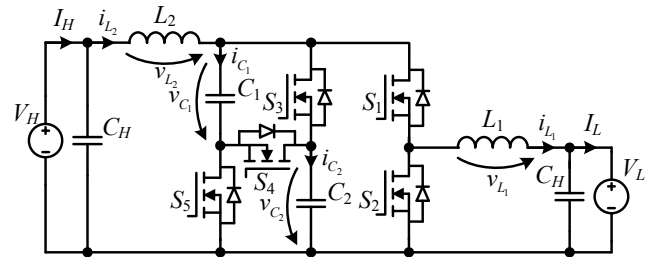


Fig. 1. The Bidirectional Hybrid Switched Capacitor (BHSC) converter topology.

### B. BHSC Operation mode

The BHSC converter can be viewed as either a buck converter from the high voltage ( $V_H$ ) perspective, or as a boost converter from the low voltage ( $V_L$ ) perspective. The switched capacitive cell is therefore connected at the input of the buck side, or at the output of the boost side. In the following pages the buck mode is presented in diagrams, the boost mode being similar, with the only difference being in the sign of the currents.

The two switching states can be observed in Fig. 2 and Fig. 3, and are defined by the  $t_{on}$  and  $t_{off}$  periods. Only one driving signal is needed for the transistors, applied directly to  $S_1$ ,  $S_3$  and  $S_5$  transistor, and then inverted to drive  $S_2$  and  $S_4$ , resulting in a simpler control.

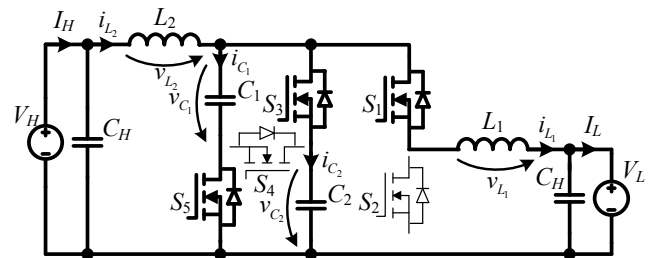


Fig. 2. BHSC equivalent schematic during  $t_{on}$  switching period.

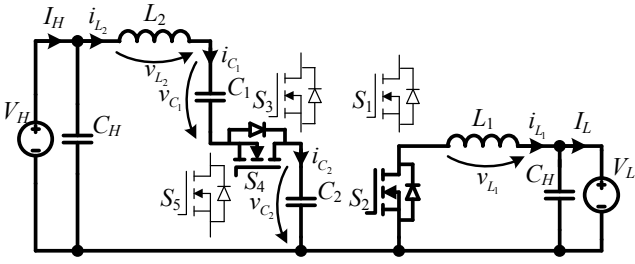


Fig. 3. BHSC equivalent schematic during  $t_{off}$  switching period.

In buck mode ( $i_{L1} > 0$ ) the two capacitors from the switching cells are discharged in parallel to the low voltage source,  $V_L$ , during  $t_{on}$ . The  $i_{L2}$  current also charges the capacitors, but it is much smaller than the discharge current so it can be neglected. The capacitors are then charged in series from the  $V_H$  voltage during  $t_{off}$ .

### C. Analytical description

Few presumptions are made in order to simplify the analysis: all components are ideal; the capacitors are considered large enough in order to obtain a negligible voltage ripple and the converter is operating in steady state.

The equations for the inductor voltages and for the switched capacitor currents in the two equivalent states are described in (1).

$$t_{on} : \begin{cases} v_{L1} = V_{C1} - V_L \\ v_{L2} = V_H - V_{C2} \\ i_{C1} + i_{C2} = i_{L2} - i_{L1} \end{cases} \quad t_{off} : \begin{cases} v_{L1} = -V_L \\ v_{L2} = V_H - V_{C2} - V_{C1} \\ i_{C1} = i_{C2} = i_{L2} \end{cases} \quad (1)$$

In order to simplify the equations, the two capacitors and their currents are considered identical ( $C_1 = C_2 = C_{sw}$ ) therefore (1) can be simplified as (2).

$$t_{on} : \begin{cases} v_{L1} = V_C - V_L \\ v_{L2} = V_H - V_C \\ 2 \cdot i_{C_{sw}} = i_{L2} - i_{L1} \end{cases} \quad t_{off} : \begin{cases} v_{L1} = -V_L \\ v_{L2} = V_H - 2 \cdot V_C \\ i_{C_{sw}} = i_{L2} \end{cases} \quad (2)$$

In order to obtain a good comparison between the BHSC and the conventional buck converter, the duty cycle ( $D$ ) is defined as in (3).

$$D = \frac{t_{on}}{T} = t_{on} \cdot f \quad (3)$$

By applying volt-second balance principle on the inductors, (2) is used to write (4).

$$\begin{cases} V_{L1} = D \cdot (V_C - V_L) + (1-D) \cdot (-V_L) = 0 \\ V_{L2} = D \cdot (V_H - V_C) + (1-D) \cdot (V_H - 2V_C) = 0 \end{cases} \quad (4)$$

Using (4), the switched capacitor voltage is determined in (5).

$$\begin{cases} V_{C_{sw}} = \frac{V_H}{2-D} \\ V_{C_{sw}} = \frac{V_L}{D} \end{cases} \quad (5)$$

Using (5) the relation between the high and the low voltage is determined in (6), and the duty cycle is determined in (7).

$$V_L = V_H \cdot \frac{D}{2-D} \quad (6)$$

$$D = \frac{2 \cdot V_L}{V_H + V_L} \quad (7)$$

The capacitor voltage is also determined in (8) and, as it can be observed, it has a constant voltage only dependent by the two input voltages, considering a steady state.

$$V_C = \frac{V_H + V_L}{2} \quad (8)$$

The theoretical waveforms presented in Fig. 4 are extracted from the two equivalent schematics (Fig. 2 and Fig. 3), and from the previous equations. Apart from the two inductor voltages and currents, the switched capacitor currents and voltage ripple ( $\Delta V_{C_{sw}}$ ) are also presented. The input and output voltage ripples ( $\Delta V_{C_H}$ ,  $\Delta V_{C_L}$ ) are represented considering that ideal capacitors are also used at the input ports (not shown in schematics Fig. 1 - Fig. 3). The ripple voltage representation is made by considering a constant current load at the inputs.

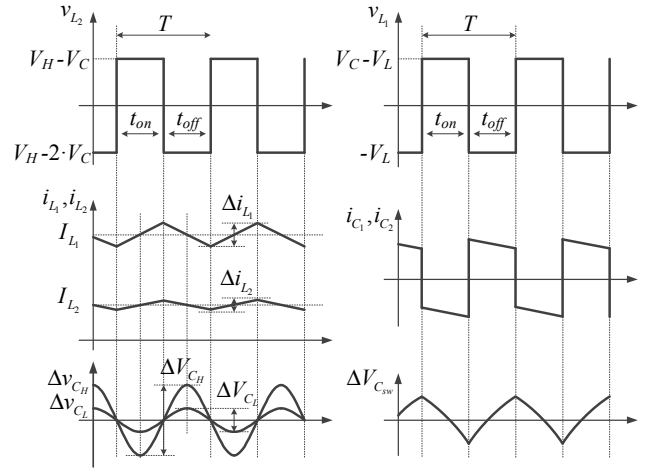


Fig. 4. Theoretical waveforms for BHSC ( $\Delta V_C$  voltages are not to scale).

### III. CONVERTER SIZING

An important aspect for any converter is its sizing and choosing its passive components, therefore the following two subsections will address this aspect.

#### A. Inductor Sizing

Considering the inductor voltages from (1), the inductor can be calculated considering  $t_{on}$  switching period and a specific value for the ripple current, therefore (9) can be written.

$$t_{on} : \begin{cases} L_1 \cdot \frac{di_{L1}}{dt} = V_{C_{sw}} - V_L \Leftrightarrow L_1 \cdot \frac{\Delta i_{L1}}{t_{on}} = V_{C_{sw}} - V_L \\ L_2 \cdot \frac{di_{L2}}{dt} = V_H - V_{C_{sw}} \Leftrightarrow L_2 \cdot \frac{\Delta i_{L2}}{t_{on}} = V_H - V_{C_{sw}} \end{cases} \quad (9)$$

Based on (9), the inductor values can be rewritten as in (10).

$$\begin{cases} L_1 = \frac{D \cdot T \cdot (V_{C_{sw}} - V_L)}{\Delta i_{L1}} \\ L_2 = \frac{D \cdot T \cdot (V_H - V_{C_{sw}})}{\Delta i_{L2}} \end{cases} \quad (10)$$

In order to compare this topology to other topologies, the design of the passive components is done considering a percentage ripple ( $\Delta i_{Lp}$ ) which is used to calculate the inductor ripple as in (11). Based on (5), (10) and (11) the inductor values can be calculated as in (12).

$$\begin{cases} \Delta i_{L1} = \Delta i_{Lp} I_{L1} \\ \Delta i_{L2} = \Delta i_{Lp} I_{L2} \end{cases} \quad (11)$$

$$\begin{cases} L_1 = \frac{V_L \cdot (V_H - V_L)}{\Delta i_{Lp} \cdot f \cdot I_L \cdot (V_H + V_L)} \\ L_2 = \frac{V_H \cdot (V_H - V_L)}{\Delta i_{Lp} \cdot f \cdot I_L \cdot (V_H + V_L)} \end{cases} \quad (12)$$

### B. Capacitors Sizing

Capacitor sizing is done similar to the inductor sizing. First, (13) is used, to show the dependency between currents and voltages. The difference here is that the capacitor currents are not constant so the integral must be calculated in (14).

$$\begin{cases} C_{sw} \cdot \frac{dv_{C_{sw}}}{dt} = \frac{i_{L2} - i_{L1}}{2} \\ C_L \cdot \frac{dv_{C_L}}{dt} = i_{L1} - I_{L1} \\ C_H \cdot \frac{dv_{C_H}}{dt} = i_{L2} - I_{L2} \end{cases} \quad (13)$$

$$\begin{cases} C_{sw} = \frac{-1}{2 \cdot \Delta v_{C_{sw}}} \int_0^{t_{on}} (i_{L2} - i_{L1}) dt \\ C_L = \frac{1}{\Delta v_{C_L}} \int_{t_{on}/2}^{t_{on} + t_{off}/2} (i_{L1} - I_{L1}) dt \\ C_H = \frac{1}{\Delta v_{C_H}} \int_{t_{on}/2}^{t_{on} + t_{off}/2} (i_{L2} - I_{L2}) dt \end{cases} \quad (14)$$

As for the inductors, a ripple voltage percentage on capacitors is considered in (15).

$$\begin{cases} \Delta v_C = \Delta v_{Cp} V_{C_{sw}} \\ \Delta v_{C_L} = \Delta v_{Cp} V_{C_L} \\ \Delta v_{C_H} = \Delta v_{Cp} V_{C_H} \end{cases} \quad (15)$$

Calculating (13) by using (15) and the currents from Fig. 4, the result from (16) is obtained.

$$\begin{cases} C_{sw} = \frac{2 \cdot I_L \cdot V_L \cdot (V_H - V_L)}{\Delta v_{Cp} \cdot f \cdot V_H \cdot (V_H + V_L)^2} \\ C_L = \frac{\Delta i_{Lp} \cdot I_L}{8 \cdot \Delta v_{Cp} \cdot f \cdot V_L} \\ C_H = \frac{\Delta i_{Lp} \cdot I_L \cdot V_L}{8 \cdot \Delta v_{Cp} \cdot f \cdot V_H^2} \end{cases} \quad (16)$$

It is important to note that the values obtained here for the capacitor values will not necessarily be used in the final design because instabilities might occur, and this aspect will be addressed in the following sections. Most importantly the values for the capacitors will be used for comparison to other topologies.

### C. Converter comparison

In order to compare the topology to other topologies, the total energy from inductors, total energy from capacitors, and total device switch stress is used as metrics. The total energy from the passive elements is more or less proportional to the cost and volume. The total switch stress provides information about the cost of the switches and the switch losses, therefore the efficiency.

The inductor energy calculated in (17). The total inductor energy is given in (19), considering the previous aspects.

$$\begin{cases} W_{L1} = \frac{L_1 \cdot I_{L1}^2}{2} = \frac{I_L \cdot V_L \cdot \left(\frac{V_H - V_L}{2} - \frac{V_L}{2}\right)}{\Delta i_{Lp} \cdot f \cdot (V_H + V_L)} \\ W_{L2} = \frac{L_2 \cdot I_{L2}^2}{2} = \frac{I_L \cdot V_L^2 \cdot (V_H - V_L)}{2 \cdot \Delta i_{Lp} \cdot f \cdot V_H \cdot (V_H + V_L)} \end{cases} \quad (17)$$

$$W_{L_{tot}} = W_{L1} + W_{L2} = \frac{I_L \cdot V_L \cdot (V_H - V_L)}{2 \cdot \Delta i_{Lp} \cdot f \cdot V_H} \quad (18)$$

The capacitor energies are calculated as in (20) and the result is given in (21). The capacitors from the two inputs ( $C_H$  and  $C_L$ ) give the same calculated energy, because of similar parameters and sizing equations.

$$\begin{cases} W_{C_{sw}} = \frac{C_{sw} \cdot V_{C_{sw}}^2}{2} \\ W_{C_L} = \frac{C_L \cdot V_L^2}{2} \\ W_{C_H} = \frac{C_H \cdot V_H^2}{2} \end{cases} \quad (19)$$

$$\begin{cases} W_{C_{sw}} = \frac{I_L \cdot V_L \cdot (V_H - V_L)}{4 \cdot \Delta v_{Cp} \cdot f \cdot V_H} \\ W_{C_L} = W_{C_H} = \frac{\Delta i_{Lp} \cdot I_L \cdot V_L}{16 \cdot \Delta v_{Cp} \cdot f} \end{cases} \quad (20)$$

The total capacitor energy is calculated as in (22) and the result is given in (23).

$$W_{C_{tot}} = 2 \cdot W_{C_{sw}} + W_{C_L} + W_{C_H} \quad (21)$$

$$W_{C_{tot}} = \frac{I_L \cdot V_L \cdot (V_H \cdot (4 + \Delta i_{Lp}) - 4 \cdot V_L)}{4 \cdot \Delta v_{Cp} \cdot f \cdot V_H} \quad (22)$$

The total switch stress is calculated as the product between the maximum voltage and maximum current on each switching device, and is used as metrics for comparison between different topologies, and is calculated as in (24).

$$S_{Total} = \sum_{j=1}^5 V_{Sj} I_{Sj} \quad (23)$$

To calculate the total switch stress, the maximum voltage and currents on the switching devices are expressed in (25). The result of the calculation are given in (26).

$$\begin{cases} V_{S1} = V_H + V_L \\ V_{S2} = V_{S3} = V_{S4} = \frac{V_H + V_L}{2} \end{cases} \begin{cases} I_{S1} = I_{S2} = I_L \\ I_{S3} = I_{S5} = \frac{I_H - I_L}{2} \\ I_{S4} = I_H \end{cases} \quad (24)$$

$$S_{Total} = \frac{I_L (V_H + V_L)^2}{V_H} \quad (25)$$

In order to have a better understanding of the resulting calculations from (18), (22) and (25), and in order to compare the proposed topology to the quadratic converter from [17] and the conventional buck/boost, the relations are divided with the corresponding results from the conventional converter, and graphically represented in Fig. 5. The voltages were chosen to be  $V_H=400V$ ,  $V_L$  ranging from 20V to 100V, and  $\Delta i_{Lp} = 20\%$  which is common for inductors, or other optimal values can be used [18]. From these results it can be observed that the BHSC converter achieves a better conversion ratio than the conventional converter using the same passive components, and that it has a lower total stress on the active switches, even if it has a larger number of switches. Also, over a wide operating range the BHSC needs smaller passive and active components than the quadratic converter.

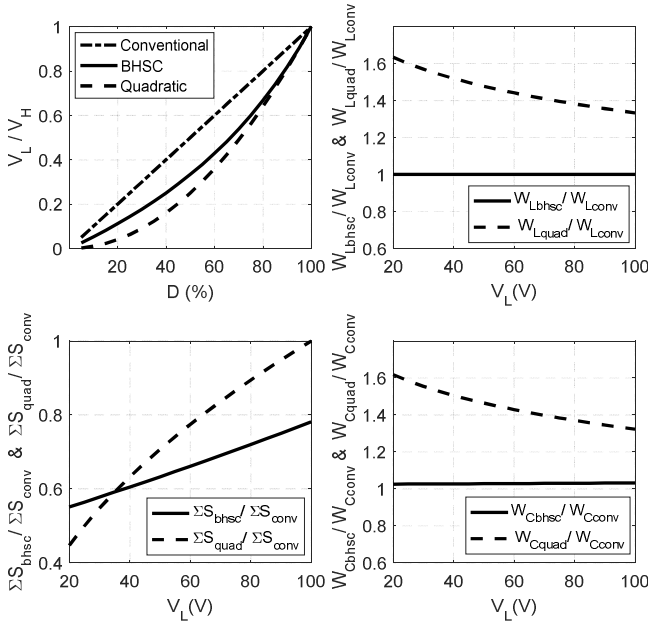


Fig. 5. BHSC comparison with the conventional bidirectional Buck/Boost converter [19] and a Quadratic converter [17] ( $V_H=400V$ ).

The quadratic converter has the best conversion ratio, followed by the BHSC and then the conventional converter, but it needs larger inductors, capacitors and more expensive switches in order to achieve this characteristic.

#### IV. STABILITY ANALYSIS

Because this topology has a larger number of passive components, therefore is a higher order system, it is important to analyze the stability by mathematical and simulation means, prior to the final design stage. The capacitor values can be calculated as in (16), but as it is seen in [20] and [11], some converters might behave as a non-minimum-phase system or their control performance might be improved by appropriate hardware design.

In order to make the stability analysis the SSA method is used. To obtain the mathematical model, the schematic from Fig. 6, including the parasitic resistors and input capacitors ( $C_H, C_L$ ), is used. The two equivalent switching schematics are presented in Fig. 7 and Fig. 8, for the  $t_{on}$  and  $t_{off}$  periods respectively. Considering the state ( $x$ ) and the input ( $u$ ) vectors as in (28), the state space representation for the two switching periods can be expressed as in (27) (where  $i = 1$  for  $t_{on}$  or 2 for  $t_{off}$ ). The  $A_i$  and  $B_i$  matrixes are defined in (29), and their elements from (30) to (46).

$$\dot{x} = A_i \cdot x + B_i \cdot u \quad (26)$$

$$x^T = [i_{L1} \quad i_{L2} \quad v_{C_{sw}} \quad v_{C_L} \quad v_{C_H}] \quad u = \begin{bmatrix} V_L \\ V_H \end{bmatrix} \quad (27)$$

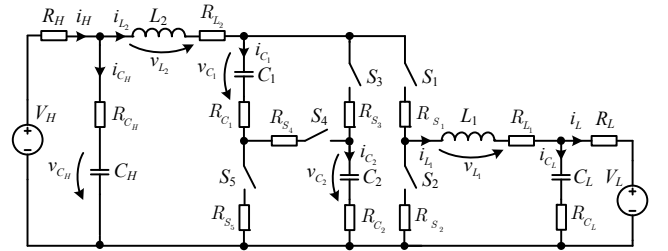


Fig. 6. BHSC schematic with parasitic components.

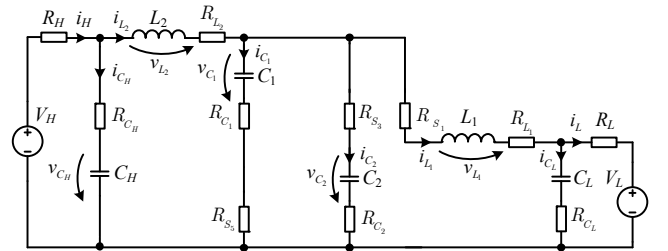


Fig. 7. BHSC schematic with parasitic components during  $t_{on}$ .

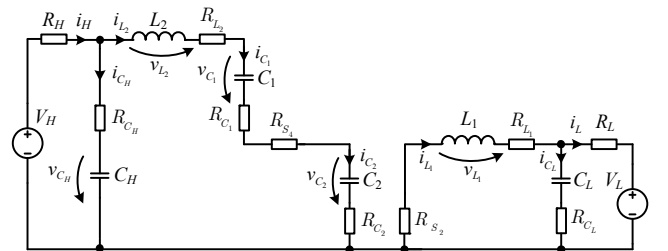


Fig. 8. BHSC schematic with parasitic components during  $t_{off}$ .

$$A_i = \begin{bmatrix} a_{11i} & a_{12i} & a_{13i} & a_{14i} & 0 \\ a_{21i} & a_{22i} & a_{23i} & 0 & a_{25i} \\ a_{31i} & a_{32i} & 0 & 0 & 0 \\ a_{41i} & 0 & 0 & a_{44i} & 0 \\ 0 & a_{52i} & 0 & 0 & a_{55i} \end{bmatrix} \quad B_i = \begin{bmatrix} b_{11i} & 0 \\ 0 & b_{22i} \\ 0 & 0 \\ b_{41i} & 0 \\ 0 & b_{52i} \end{bmatrix} \quad (28)$$

$$a_{11i} = - \left( \frac{R_{C_{sw}} + R_{L_1} + R_{S_1} + \frac{R_{S_3}}{2} + \frac{R_{C_L} \cdot R_L}{R_{C_L} + R_L}}{L_1} \right) \quad (29)$$

$$a_{12i} = \frac{R_{C_{sw}} + R_{S_3}}{2 \cdot L_1}; \quad a_{13i} = \frac{1}{L_1}; \quad a_{14i} = \frac{-R_L}{L_1 \cdot (R_{C_L} + R_L)} \quad (30)$$

$$a_{21i} = \frac{R_{C_{sw}} + R_{S_3}}{2 \cdot L_2}; \quad a_{23i} = -\frac{1}{L_2}; \quad a_{25i} = \frac{R_H}{L_2 \cdot (R_{C_H} + R_H)} \quad (31)$$

$$a_{22i} = - \left( \frac{R_{C_{sw}} + R_{L_2} + \frac{R_{S_3}}{2} + \frac{R_{C_H} \cdot R_H}{R_{C_H} + R_H}}{L_2} \right) \quad (32)$$

$$a_{31i} = -\frac{1}{2 \cdot C_{sw}}; \quad a_{32i} = -a_{31i}; \quad a_{41i} = \frac{R_L}{C_L \cdot (R_{C_L} + R_L)} \quad (33)$$

$$a_{44i} = \frac{-1}{C_L \cdot (R_{C_L} + R_L)}; \quad a_{52i} = \frac{-R_H}{C_H \cdot (R_{C_H} + R_H)} \quad (34)$$

$$a_{55i} = \frac{-1}{C_H \cdot (R_{C_H} + R_H)} \quad (35)$$

$$b_{11i} = \frac{-R_{C_L}}{L_1 \cdot (R_{C_L} + R_L)}; \quad b_{22i} = \frac{R_{C_H}}{L_2 \cdot (R_{C_H} + R_H)} \quad (36)$$

$$b_{41i} = \frac{1}{C_L \cdot (R_{C_L} + R_L)}; \quad b_{52i} = \frac{1}{C_H \cdot (R_{C_H} + R_H)} \quad (37)$$

$$a_{112} = - \left( \frac{R_{L_1} + R_{S_2} + \frac{R_{C_L} \cdot R_L}{R_{C_L} + R_L}}{L_1} \right); \quad a_{122} = 0; \quad a_{132} = 0 \quad (38)$$

$$a_{142} = \frac{-R_L}{L_1 \cdot (R_{C_L} + R_L)}; \quad a_{212} = 0; \quad a_{232} = -\frac{2}{L_2} \quad (39)$$

$$a_{222} = - \left( \frac{2 \cdot R_{C_{sw}} + R_{L_2} + R_{S_4} + \frac{R_{C_H} \cdot R_H}{R_{C_H} + R_H}}{L_2} \right) \quad (40)$$

$$a_{252} = \frac{R_H}{L_2 \cdot (R_{C_H} + R_H)}; \quad a_{312} = 0; \quad a_{322} = \frac{1}{C_{sw}} \quad (41)$$

$$a_{412} = \frac{R_L}{C_L \cdot (R_{C_L} + R_L)}; \quad a_{442} = \frac{-1}{C_L \cdot (R_{C_L} + R_L)} \quad (42)$$

$$a_{522} = \frac{-R_H}{C_H \cdot (R_{C_H} + R_H)}; \quad a_{552} = \frac{-1}{C_H \cdot (R_{C_H} + R_H)} \quad (43)$$

$$b_{112} = \frac{-R_{C_L}}{L_1 \cdot (R_{C_L} + R_L)}; \quad b_{222} = \frac{R_{C_H}}{L_2 \cdot (R_{C_H} + R_H)} \quad (44)$$

$$b_{412} = \frac{1}{C_L \cdot (R_{C_L} + R_L)}; \quad b_{522} = \frac{1}{C_H \cdot (R_{C_H} + R_H)} \quad (45)$$

Taking a variable duty cycle into account ( $d$ ), the average model of the converter can be described as in (47).

$$\dot{x} = (A_1 \cdot d + A_2 \cdot (1-d)) \cdot x + (B_1 \cdot d + B_2 \cdot (1-d)) \cdot u \quad (46)$$

Linearizing the system around a steady state duty cycle  $D$  for a small signal variation  $\tilde{d}$ , the system from (48) is obtained, with the equivalent matrixes described in (49). The  $C_e$  matrix can be either  $[1 \ 0 \ 0 \ 0 \ 0]$  or  $[0 \ 1 \ 0 \ 0 \ 0]$ , in order to express the desired transfer function for one of the two inductor currents in (50), which are needed to control the bidirectional converter.

$$\begin{cases} \dot{\tilde{x}} = A_e \cdot \tilde{x} + B_e \cdot \tilde{d} \\ \tilde{y} = C_e \cdot \tilde{x} \end{cases} \quad (47)$$

$$\begin{aligned} A_e &= (A_1 \cdot D + A_2 \cdot (1-D)) \\ B_e &= [(A_1 - A_2) \cdot X + (B_1 - B_2) \cdot u] \end{aligned} \quad (48)$$

$$H_1(s) = \frac{\tilde{i}_{L_1}(s)}{\tilde{d}(s)}; \quad H_2(s) = \frac{\tilde{i}_{L_2}(s)}{\tilde{d}(s)} \quad (49)$$

The above mentioned transfer functions can be obtained by calculating (51).

$$\tilde{y} = C_e \cdot (s \cdot I - A_e)^{-1} \cdot B_e \cdot \tilde{d} \quad (50)$$

Initial design parameters and initial results are set in TABLE I.

TABLE I. INITIAL DESIGN PARAMETERS

Element	Design values		Element	Calculated values	
	Value	Unit		Value	Unit
$V_H$	400	V	$L_1$	75	$\mu\text{H}$
$V_L$	100	V	$L_2$	300	$\mu\text{H}$
$I_L$	50	A	$C_{sw}$	18.7	$\mu\text{F}$
$\Delta i_{Lp}$	20	%	$C_L$	7.8	$\mu\text{F}$
$\Delta v_{Cp}$	2	%	$C_H$	0.48	$\mu\text{F}$
$f_{sw}$	80	kHz	$D$	40	%

Unfortunately the stability of the converter is affected if the capacitors from the previous table are used because of the low ESR ( $\approx 1.3 \text{ m}\Omega$ ) of the  $C_{sw}$ , which introduce right half-plane zero (around  $1350.153 \pm 14782.163i$ ) in  $H_1(s)$ . This case is also studied in [20], and in order to avoid it, electrolytic capacitors are chosen for the design, with the final values from TABLE II.

TABLE II. SELECTED COMPONENTS (CASE A)

Part	Specifications					
	Value	Unit	ESR	ESR value	Unit	Component
$L_1$	100	$\mu\text{H}$	$R_{L_1}$	20	$\text{m}\Omega$	2x DEHF-42/0,047/50
$L_2$	400	$\mu\text{H}$	$R_{L_2}$	53	$\text{m}\Omega$	DEHF-42/0,47/16
$C_{sw}$	20	$\text{mF}$	$R_{C_{sw}}$	15.4	$\text{m}\Omega$	ALC70(1)202EL350
$C_L$	10	$\text{mF}$	$R_{C_L}$	34	$\text{m}\Omega$	ALC70103EH100
$C_H$	0.22	$\text{mF}$	$R_{C_H}$	328	$\text{m}\Omega$	ALC70221BD400

Taking the values from the previous table, the transfer functions can be calculated, and the new poles and zeros of the system can be extracted in TABLE III. In order to further reduce the oscillations that might appear the introduction of an additional resistor is considered, so that  $R_{C_{sw}} = 0.12\Omega$  (for Case B), and the new poles and zeros are presented in TABLE IV. The bode diagram of the two transfer functions,  $H_1(s)$  and  $H_2(s)$ , for the two cases, are presented in Fig. 9 and Fig. 10 respectively. It can be observed from the new values of the poles that the converter will have smaller oscillations with an increased ESR, but this will also increase significantly the losses (approximately 1% more losses in the ESR of  $C_{sw}$ ). Because of this the controller is designed with the capacitors from the case A, and a low-pass filter is used for the reference current ( $f_c=100\text{ Hz}$ ), as implemented in [11]. The current through  $L_1$  inductor is used for control, as it has higher current values and a higher dynamic.

The chosen current controller is a PI controller, and its transfer function is presented in (52). The frequency response of  $C(s) \cdot H_1(s)$  from Fig. 11 shows good stability using this controller, obtaining a phase margin of 87.2 degrees.

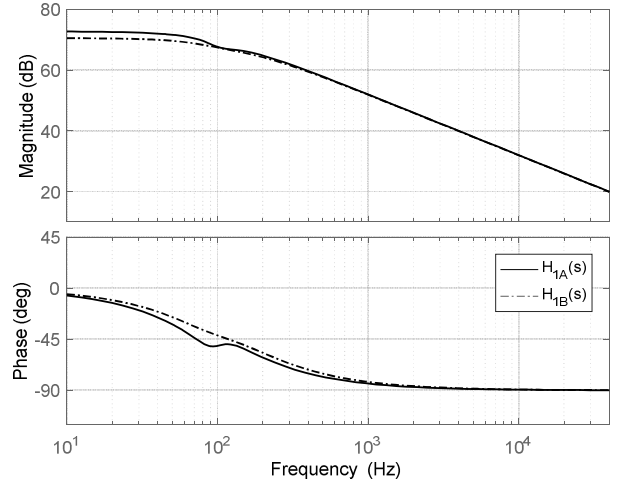
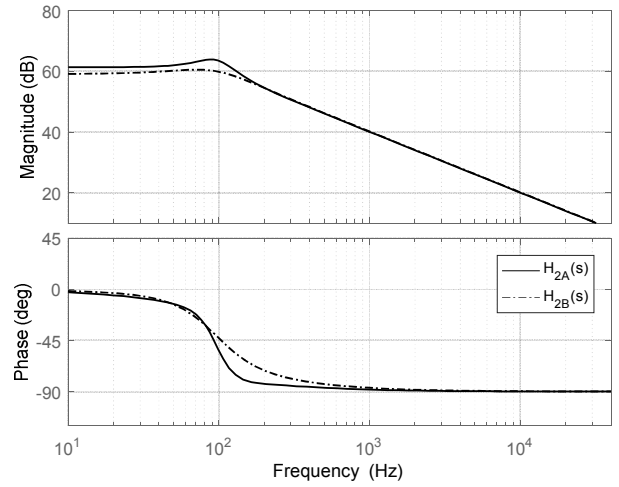
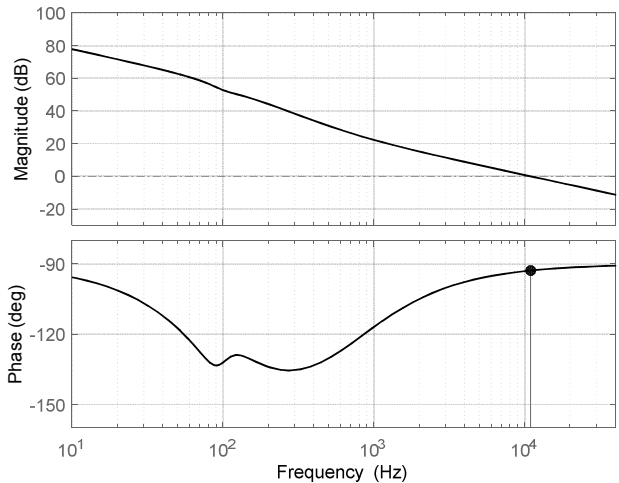
$$C(s) = \frac{0.02754 \cdot (s + 4075)}{s} \quad (51)$$

TABLE III. SYSTEM WITH COMPONENTS A.

Element	Pole and Zero values	
	Pole and Zero values for set A of capacitors	
$H_1(s)$ Poles	-12872.11578, -2240.59207, -194.02532 $\pm$ 579.94806i, -622.67995	
$H_1(s)$ Zeros	-12872.10936, -2272.72727, -163.15708 $\pm$ 608.53028i	
$H_2(s)$ Poles	-12872.11578, -2240.59207, -194.02532 $\pm$ 579.94806i, -622.67995	
$H_2(s)$ Zeros	-12876.64177, -2241.63320, -407.04398 $\pm$ 511.63483i	

TABLE IV. SYSTEM WITH COMPONENTS B.

Element	Pole and Zero values	
	Pole and Zero values for 1 <sup>st</sup> set of capacitors	
$H_1(s)$ Poles	-12871.97709, -2235.19829, -390.80492 $\pm$ 457.04867i, -829.11094	
$H_1(s)$ Zeros	-12871.94915, -2272.72727, -378.86668 $\pm$ 504.53682i	
$H_2(s)$ Poles	-12871.97709, -2235.19829, -829.11094, -390.80492 $\pm$ 457.04867i	
$H_2(s)$ Zeros	-12876.64177, -2230.04382, -628.40118 $\pm$ 167.60799i	


 Fig. 9. Bode diagram for the transfer functions of  $H_1(s)$  for the two capacitor sets: A and B.

 Fig. 10. Bode diagram for the transfer functions of  $H_2(s)$  for the two capacitor sets: A and B.

 Fig. 11. Frequency response of the converter with the designed controller  $C(s) \cdot H_1(s)$  (PM = 87.2 deg,  $f_i = 11\text{ kHz}$ ).

## V. SIMULATION RESULTS

The results, obtained from PSIM software simulations, show a good operation of the converter under various conditions.

For the first case, with the capacitors from A, the results are shown in Fig. 12 and Fig. 13. First, a current reference of  $\pm 50A$  is applied to test a large step variation. The  $I_{L_1}$  current has no overshoot and the  $I_{L_2}$  current has little oscillations.

Small oscillations are also present on the switched capacitors. On the second figure a  $\pm 10A$  reference is applied, and here it can be observed that the oscillations are largely reduced.

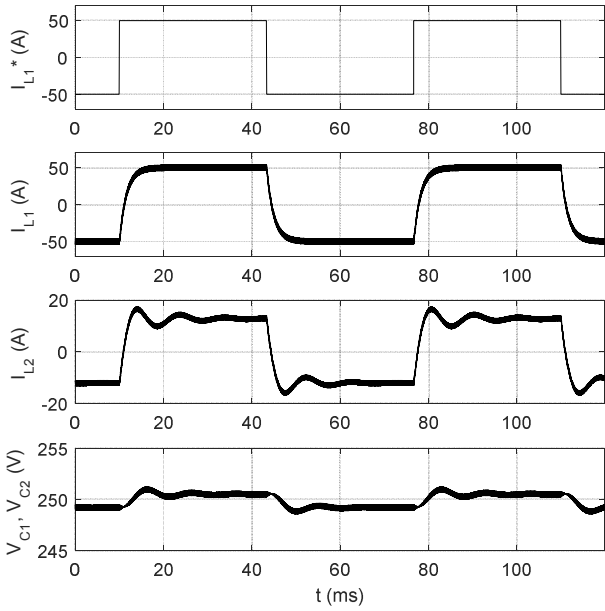


Fig. 12. Simulation results for  $I_{L_1}^* = \pm 50A$ ,  $V_H=400V$ ,  $V_L=100V$  for Case A capacitors.

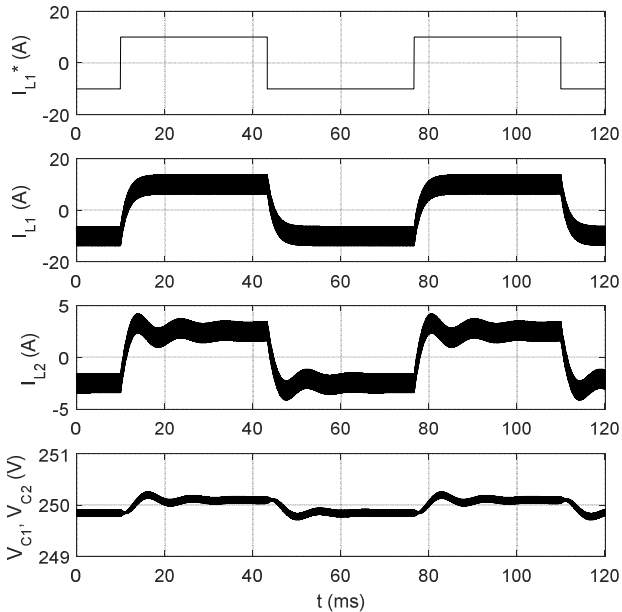


Fig. 13. Simulation results for  $I_{L_1}^* = \pm 10A$ ,  $V_H=400V$ ,  $V_L=100V$  for Case A capacitors.

In the second case, with the additional ESR (B), the same conditions are tested. In Fig. 14 a reference of  $\pm 50A$ , is applied, and here it can be observed that the overshoot in the  $I_{L_2}$  current is much lower, and the settling time for the oscillations is shorter. The same are correct for the  $\pm 10A$  reference. The reduced oscillations are also present in this case. Another important aspect to mention is the increased voltage ripple on the capacitors due to the increased ESR.

A close-up on the steady state waveforms is also shown in Fig. 16, and it shows a good correspondence with the expected results.

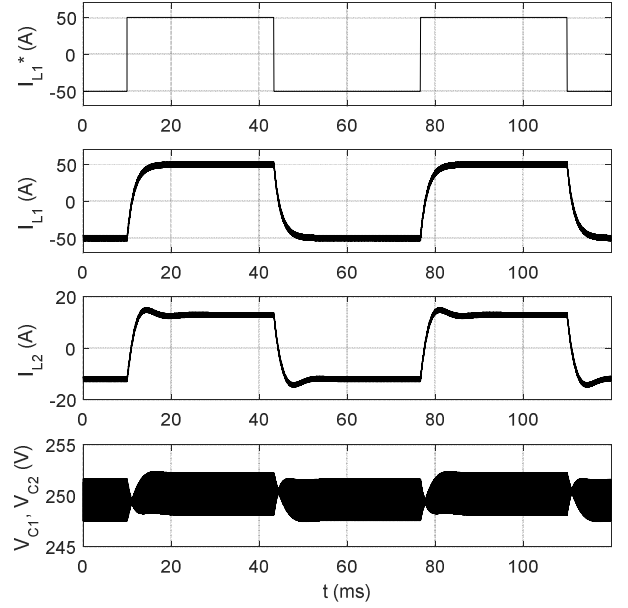


Fig. 14. Simulation results for  $I_{L_1}^* = \pm 50A$ ,  $V_H=400V$ ,  $V_L=100V$  for Case B capacitors.

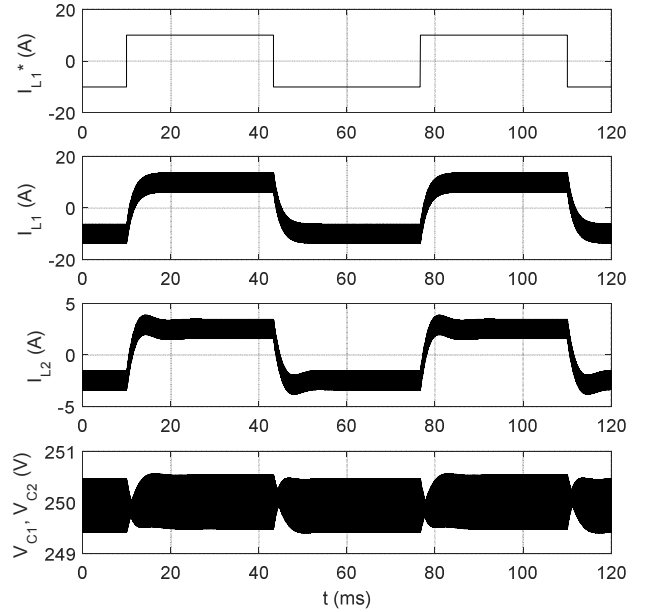


Fig. 15. Simulation results for  $I_{L_1}^* = \pm 10A$ ,  $V_H=400V$ ,  $V_L=100V$  for Case B capacitors.

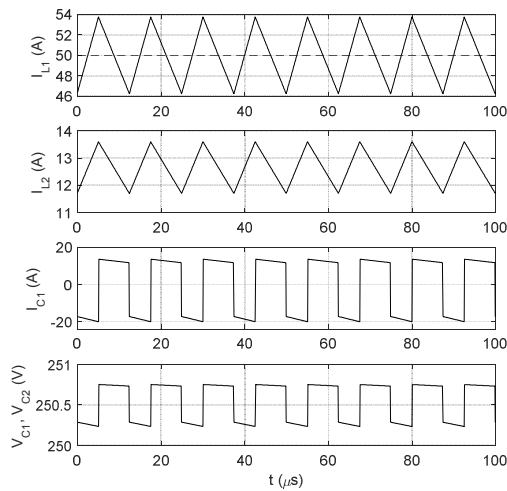


Fig. 16. Close up on the simulation waveforms,  $I_{L_1}^* = 50A$ ,  $V_H = 400V$ ,  $V_L = 100V$  for Case A capacitors.

## VI. CONCLUSIONS

This paper presented a new bidirectional DC-DC converter topology, which can achieve a high conversion ratio with the help of a switched capacitor cell. Apart from the increased conversion ratio, the benefits of this topology also include smaller passive components, lower stress on the active devices, lower ripple current at the inputs and a common ground between the two ports. The stability of the converter was analyzed with emphasis on the design of the passive components, in order to achieve a stable design prior to the actual construction of the converter. The simulation results confirm the performances and the stability of the proposed converter.

## ACKNOWLEDGMENT

This work was supported by a grant of the Romanian Ministry of Research and Innovation, CCCDI – UEFISCDI, project number PN-III-P1-1.2-PCCDI-2017- 0391 / CIA\_CLIM – “Smart buildings adaptable to the climate change effects”, within PNCDI III.

This work was also supported by a grant of the Romanian Ministry of Research and Innovation, project number 10PFE/16.10.2018, PERFORM-TECH-UPT - *The increasing of the institutional performance of the Polytechnic University of Timișoara by strengthening the research, development and technological transfer capacity in the field of "Energy, Environment and Climate Change"*, within Program 1 - Development of the national system of Research and Development, Subprogram 1.2 - Institutional Performance - Institutional Development Projects - Excellence Funding Projects in RDI, PNCDI III.

## REFERENCES

- [1] Y. Karimi, H. Oraee, M. S. Golsorkhi, and J. M. Guerrero, “Decentralized Method for Load Sharing and Power Management in a PV/Battery Hybrid Source Islanded Microgrid,” *IEEE Transactions on Power Electronics*, vol. 32, no. 5, pp. 3525–3535, May 2017.
- [2] X. Zhao, X. Wu, Y. Li, and H. Tian, “Energy management strategy of multiple supercapacitors in an autonomous DC microgrid using adaptive virtual impedance,” in *2016 IEEE 7th International Symposium on Power Electronics for Distributed Generation Systems (PEDG)*, 2016, pp. 1–8.
- [3] Y. Zhang and Y. Li, “Energy management strategy for supercapacitor in autonomous DC microgrid using virtual impedance,” in *2015 IEEE Applied Power Electronics Conference and Exposition (APEC)*, 2015, pp. 725–730.
- [4] A. S. Morais and L. A. C. Lopes, “Interlink Converters in DC nanogrids and its effect in power sharing using distributed control,” in *2016 IEEE 7th International Symposium on Power Electronics for Distributed Generation Systems (PEDG)*, 2016, pp. 1–7.
- [5] J. Ma, M. Zhu, X. Cai, and Y. W. Li, “Configuration and operation of DC microgrid cluster linked through DC-DC converter,” in *2016 IEEE 11th Conference on Industrial Electronics and Applications (ICIEA)*, 2016, pp. 2565–2570.
- [6] B. Lee, J. Kim, S. Kim, and J. Lee, “An Isolated/Bidirectional PWM Resonant Converter for V2G(H) EV On-Board Charger,” *IEEE Transactions on Vehicular Technology*, vol. 66, no. 9, pp. 7741–7750, Sep. 2017.
- [7] P. He and A. Khaligh, “Comprehensive Analyses and Comparison of 1 kW Isolated DC-DC Converters for Bidirectional EV Charging Systems,” *IEEE Transactions on Transportation Electrification*, vol. 3, no. 1, pp. 147–156, Mar. 2017.
- [8] S. Dusmez, A. Hasanzadeh, and A. Khaligh, “Loss analysis of non-isolated bidirectional DC/DC converters for hybrid energy storage system in EVs,” in *2014 IEEE 23rd International Symposium on Industrial Electronics (ISIE)*, 2014, pp. 543–549.
- [9] Y. Zhang, Y. Gao, L. Zhou, and M. Sumner, “A Switched-Capacitor Bidirectional DC-DC Converter With Wide Voltage Gain Range for Electric Vehicles With Hybrid Energy Sources,” *IEEE Transactions on Power Electronics*, vol. 33, no. 11, pp. 9459–9469, Nov. 2018.
- [10] D. Hulea, B. Fahimi, N. Muntean, and O. Cornea, “High Ratio Bidirectional Hybrid Switched Inductor Converter Using Wide Bandgap Transistors,” in *2018 20th European Conference on Power Electronics and Applications (EPE'18 ECCE Europe)*, 2018, p. P.1-P.10.
- [11] O. Cornea, G. Andreescu, N. Muntean, and D. Hulea, “Bidirectional Power Flow Control in a DC Microgrid Through a Switched-Capacitor Cell Hybrid DC-DC Converter,” *IEEE Transactions on Industrial Electronics*, vol. 64, no. 4, pp. 3012–3022, Apr. 2017.
- [12] F. S. Garcia, J. A. Pomilio, and G. Spiazzi, “Comparison of non-insulated, high-gain, high-power, step-up DC-DC converters,” in *2012 Twenty-Seventh Annual IEEE Applied Power Electronics Conference and Exposition (APEC)*, 2012, pp. 1343–1347.
- [13] B. Axelrod, Y. Berkovich, and A. Ioinovici, “Switched-Capacitor/Switched-Inductor Structures for Getting Transformerless Hybrid DC-DC PWM Converters,” *IEEE Transactions on Circuits and Systems I: Regular Papers*, vol. 55, no. 2, pp. 687–696, Mar. 2008.
- [14] N. Muntean, O. Cornea, O. Pelan, and C. Lascu, “Comparative evaluation of buck and hybrid buck DC-DC converters for automotive applications,” in *2012 15th International Power Electronics and Motion Control Conference (EPE/PEMC)*, 2012, p. DS2b.3-1-DS2b.3-6.
- [15] S. Li, K. M. Smedley, D. R. Caldas, and Y. W. Martins, “A hybrid bidirectional DC-DC converter for dual-voltage automotive systems,” in *2017 IEEE Applied Power Electronics Conference and Exposition (APEC)*, 2017, pp. 355–361.
- [16] P. S. Tomar, A. K. Sharma, and K. Hada, “Energy storage in DC microgrid system using non-isolated bidirectional soft-switching DC/DC converter,” in *2017 6th International Conference on Computer Applications In Electrical Engineering-Recent Advances (CERA)*, 2017, pp. 439–444.
- [17] H. Ardi, A. Ajami, F. Kardan, and S. N. Avilagh, “Analysis and Implementation of a Nonisolated Bidirectional DC-DC Converter With High Voltage Gain,” *IEEE Transactions on Industrial Electronics*, vol. 63, no. 8, pp. 4878–4888, Aug. 2016.
- [18] He Li-gao and Wu Jian, “Selection of the current ripple ratio of converters and optimal design of output inductor,” in *2010 5th IEEE Conference on Industrial Electronics and Applications*, 2010, pp. 1163–1167.
- [19] K. Tytelmaier, O. Husev, O. Veligorskyi, and R. Yershov, “A review of non-isolated bidirectional dc-dc converters for energy storage systems,” in *2016 II International Young Scientists Forum on Applied Physics and Engineering (YSF)*, 2016, pp. 22–28.
- [20] Y. Zhang, J. Liu, and X. Ma, “Using RC type damping to eliminate right-half-plane zeros in high step-up DC-DC converter with diode-capacitor network,” in *2013 IEEE ECCE Asia Downunder*, 2013, pp. 59–65.